

Modeling the seasonal variation of sea ice in the Labrador Sea with a coupled multicategory ice model and the Princeton ocean model

T. Yao, C. L. Tang, and I. K. Peterson

Ocean Sciences Division, Fisheries and Oceans Canada, Bedford Institute of Oceanography, Dartmouth, Nova Scotia, Canada

Abstract. We use a multicategory sea ice model coupled to the Princeton ocean model, which is driven by monthly climatological atmospheric forcing, to study the seasonal variation of ice cover in the Labrador Sea. Initial ocean conditions are derived from a gridded, objectively analyzed temperature-salinity data set that provides improved resolution of gradients in the vicinity of the shelf break. The model produces a realistic seasonal variation of sea ice. There is ice growth over the inner shelf and ice melt over the outer shelf and slope. Over the inner shelf, advection and diffusion decrease the ice mass; over the outer shelf, advection and diffusion increase the ice mass, which maintains the location of the ice edge. Near the offshore ice edge the melt rate exceeds 1 m per month, and the heat to melt ice together with the heat lost to the atmosphere exceeds 500 W m^{-2} . The heat lost at the ocean surface is compensated for by advection of heat from an offshore convective region. The dominant heat source for the spring retreat of ice in the south is shortwave radiation over the open water fraction.

1. Introduction

Marginal ice zones are regions of dynamic interaction between atmosphere, ice, and ocean. In the Labrador marginal ice zone the ice edge is located near the Labrador Current and its associated shelf break front. Wintertime convection in the western Labrador Sea is thought to form Labrador Intermediate Water [Clarke and Gascard, 1983]. Since the ice edge borders the convective region, it is important to clarify the processes that limit the ice extent and to examine the heat and salt fluxes in the vicinity of the ice edge.

In this study we investigate the seasonal evolution of sea ice over the Labrador shelf with a coupled ice-ocean model. Our objective is to assess the capability of the model in simulating the evolution of the ice cover and to identify model deficiencies. We examine the processes that limit the ice extent.

Labrador sea ice has been the subject of a number of studies with numerical models. Most recently, Ikeda *et al.* [1996] coupled a two-category ice model [Hibler, 1979] with the Geophysical Fluid Dynamics Laboratory (GFDL) ocean model [Bryan, 1969; Cox, 1984]. There was overall agreement with the seasonal cycle as well as with interannual variations. The results showed that shoreward advection of relatively warm offshore water is an important source of heat to melt ice. However, the model ice decayed too rapidly, partly because the two-category ice model underestimates ice concentration.

There are a number of differences between the present model and the model of Ikeda *et al.* [1996]. We have implemented a multicategory ice model and used the sigma coordinate Princeton ocean model [Blumberg and Mellor, 1987; Mellor, 1996] with its embedded turbulence closure submodel. We use a climatology from the National Centers for Environmental Prediction (NCEP)/National Center for Atmospheric Research

(NCAR) reanalysis [Kalnay *et al.*, 1996]. A major improvement should be the use of a temperature-salinity data set for the initial ocean state, which better resolves gradients in the vicinity of the shelf break [Tang and Wang, 1996].

Ice-ocean interactions on the Labrador and Newfoundland shelves have been studied using coupled ice-mixed layer models. Tang and deTracey [1998] studied the influence of sea ice on the heat and salt balance of the mixed layer and simulated the observed temperature-salinity distribution across the shelf. They concluded that the southward advection of salinity was an important factor in determining the mixed layer properties. Tang *et al.* [1999] investigated the sensitivity of sea ice to oceanic and meteorological variables and found that interannual variations of ice extent were mainly controlled by local meteorological conditions.

Remote sensing of sea ice over the Newfoundland shelf was the subject of the Labrador Ice Margin Experiment 1987 (LIMEX '87) [Carsey *et al.*, 1989]. During this experiment, onshore winds compressed the ice into a narrow band (<50 km wide) against the coast. Two distinct regimes were evident. The outer regime was subject to ocean swell and was characterized by a smaller floe diameter and greater ice thickness (from rafting of floes one over another). Drinkwater and Squire [1989] argue that different ice rheologies apply to the two regimes. The present model is unlikely to be able to simulate the shorter timescale and space scale features as revealed in the LIMEX '87 observations.

2. Model Description

2.1. Ice Model

2.1.1. Momentum balance. The momentum balance governing ice velocity \mathbf{u}_i is

$$m \frac{d}{dt} \mathbf{u}_i + m \hat{\mathbf{f}} \mathbf{k} \times \mathbf{u}_i = -m \hat{g} \nabla H + A(\boldsymbol{\tau}_a - \boldsymbol{\tau}_w) + \nabla \cdot \boldsymbol{\sigma} \quad (1)$$

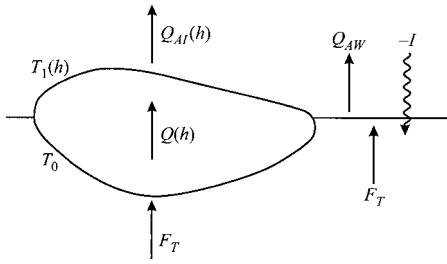


Figure 1. Schematic diagram showing heat fluxes and ice surface temperatures.

where m is the ice mass per unit area, \hat{f} is the Coriolis parameter, \hat{g} is the acceleration of gravity, ∇H is the gradient of sea surface elevation, A is the ice-covered fraction, τ_a and τ_w are the air and water stresses, respectively, and σ is the two-dimensional internal ice stress tensor. We shall neglect the acceleration term in (1). The internal ice stress is derived from the viscous plastic rheology of *Hibler* [1979] and involves a compressive ice strength

$$p = p^* \bar{h} \exp[-C(1 - A)] \quad (2)$$

where \bar{h} is a mean ice thickness and p^* and C are empirical constants (here $2.5 \times 10^4 \text{ N m}^{-2}$ and 20, respectively). Alternatives to (2) are given by *Overland and Pease* [1988] and for multicategory models by *Hibler* [1980] and *Flato and Hibler* [1995].

2.1.2. Thickness distribution. The presence of open water with ice of various thicknesses was characterized by *Thorndike et al.* [1975] with a thickness distribution $g(h)$ where $g(h)dh$ is defined as the fraction of area covered by ice between thicknesses h and $h + dh$. Ice-covered fraction A and mean ice thickness \bar{h} are defined from $g(h)$ as

$$A = \int_{0+}^{\infty} g(h) dh \quad \bar{h} = \int_0^{\infty} hg(h) dh \quad (3)$$

where the limits in the first integral are over nonzero h .

The thickness distribution satisfies a continuity equation

$$\frac{\partial}{\partial t} g + \nabla \cdot (\mathbf{u}, g) = - \frac{\partial}{\partial h} (fg) + \psi + \text{diffusion} \quad (4)$$

where $f(h)$ is the thermodynamical vertical growth rate of ice. The mechanical redistribution function ψ represents the creation of open water and ridging of ice during deformation. The redistribution process conserves ice volume. The redistribution function we use follows *Hibler* [1980] with one exception. *Hibler* proposes that ice of a given thickness ridges to a range of thicknesses; we specify that ice of a given thickness ridges to ice of a single thickness (the multiplication factor is chosen as 15). This parameterization was used by *Thorndike et al.* [1975]. *Flato and Hibler* [1995] investigate the sensitivity of the thickness distribution function to various parameterizations.

2.1.3. Ice thermodynamics. Ice thermodynamics governs the growth rate $f(h)$ in (4). Our formulation follows that of *Hibler* [1980]. The upward heat flux $Q(h)$ through ice of thickness h is

$$Q(h) = -k(T_1 - T_0)/h \quad (5)$$

where k is the conductivity of ice and T_1 and T_0 are the temperatures of the upper and lower surfaces of ice, respectively (Figure 1). The lower surface temperature T_0 is assumed to be the freezing point of seawater. The upper surface temperature T_1 is adjusted so that $Q(h)$ balances Q_{AI} , the sum of sensible and latent heat flux, and absorbed shortwave and net longwave radiation. If T_1 is found to exceed 0°C , the atmosphere-ice heat flux Q_{AI} is determined with $T_1 = 0^\circ\text{C}$. This flux melts ice at the upper surface; the melt is assumed to drain immediately into the ocean. The process is expressed as

$$\int_{0+}^{\infty} [Q_{AI}(h) - Q(h)]g(h) dh = \rho L W_{AI} \quad (6)$$

where ρ is the density of seawater, L is the latent heat of fusion, and W_{AI} is the volume flux of melt water.

The volume flux of seawater, W_{IW} , corresponding to growth or melt at the lower surface of ice is

$$\int_{0+}^{\infty} [Q(h) - F_T]g(h) dh = \rho L W_{IW} \quad (7)$$

where F_T is the heat flux out of the ocean surface (assumed to be uniform over a model grid cell). The volume flux of seawater, W_{AW} , corresponding to ice growth over the open water fraction is

$$(Q_{AW} - F_T)(1 - A) = \rho L W_{AW} \quad (8)$$

where Q_{AW} is the atmosphere-ocean heat flux excluding shortwave radiation I , which is absorbed in the water column. When the left-hand side of (8) is negative, “melting” of open water is implied; in this case the equivalent heat is redistributed to melt the remaining ice. The integrals in (6) and (7) over the range h to $h + dh$ give the growth rate $f(h)$ in the continuity equation (4). The rate of total ice growth is given by $(W_{AI} + W_{IW} + W_{AW})\rho/\rho_i$ where ρ_i is the density of ice.

The presence of a snow layer is important for the heat exchange with the atmosphere; however, it is difficult to model. Here we specify that thin ice ($h < 0.2 \text{ m}$) is bare ice with an albedo of 0.5 and thicker ice is snow-covered with an albedo of 0.75. This compares with the ocean albedo of 0.1. The presence of snow has no other effect except to modify the albedo.

2.2. Ice-Ocean Coupling

Heat and salt fluxes at the ice-ocean interface are governed by the boundary processes discussed by *Mellor and Kantha* [1989]. In grid cells in which ice is present the heat flux out of the ocean is

$$F_T = -\rho c_p C_{Tz}(T_0 - T) \quad (9)$$

where c_p is the specific heat of seawater and T is the ocean temperature at the uppermost model grid (in our model the midpoint of the uppermost ocean layer). The heat transfer coefficient C_{Tz} is given by

$$C_{Tz} = \frac{u_*}{P_{rt} \ln(-z/z_0)/\kappa + B_T} \quad (10)$$

$$B_T = b(z_0 u_* / \nu)^{1/2} P_{rt}^{2/3}$$

where u_* is the friction velocity, P_{rt} is a turbulent Prandtl number, z is the vertical coordinate corresponding to the tem-

perature T , z_0 is the roughness length, and κ is the von Karman constant. The molecular sublayer correction is represented by B_T where P_r is a molecular Prandtl number, ν is the kinematic viscosity, and b is an empirical constant (here taken as 3). The salt flux out of the ocean is

$$F_S = (W_{AI} + W_{IW} + W_{AW})(S_I - S) + (1 - A)S(\dot{P} - \dot{E}) \quad (11)$$

where S_I is the salinity of ice (chosen here as 5), S is the salinity at the uppermost model grid point, and $(\dot{P} - \dot{E})$ is the volume flux of precipitation minus evaporation.

Analogous to the heat flux (9), the salt flux is defined

$$F_S = -C_{S_z}(S_0 - S) \quad (12)$$

where S_0 is the salinity at the ice-ocean interface. The salt transfer coefficient C_{S_z} is

$$C_{S_z} = \frac{u_*}{P_r \ln(-z/z_0)/\kappa + B_S} \quad (13)$$

$$B_S = b(z_0 u_* / \nu)^{1/2} S_c^{2/3}$$

where S_c is a Schmidt number. Since $S_c = 2432$ and $P_r = 12.9$, $C_{T_z} > C_{S_z}$. This can lead to the production of frazil ice in the water column as discussed by Mellor and Kantha [1989]. Frazil ice is immediately added to the floating ice.

Given the heat flux $Q(h)$ from the ice model, (7)–(12) are solved for F_T , F_S , $(W_{AI} + W_{IW} + W_{AW})$, T_0 , and S_0 under the constraint that T_0 is the freezing point of seawater at salinity S_0 . In grid cells that are ice-free the constraint on T_0 is relaxed, and F_T is set equal to Q_{AW} .

The ice-water stress is

$$\frac{1}{\rho} \tau_{iw} = \frac{\kappa u_*}{\ln(z/z_0)} (\mathbf{u}_i - \mathbf{u}) \quad (14)$$

where \mathbf{u} is the ocean velocity at the uppermost model grid.

2.3. Ocean Model

The ocean model in the study is the Princeton ocean model [Blumberg and Mellor, 1987; Mellor, 1996]. The model has a free surface, uses sigma coordinates in the vertical, and employs a mode time split. The model contains an embedded second-order turbulence closure submodel. Horizontal diffusion is along sigma surfaces and uses a Smagorinsky diffusivity. Prognostic variables are velocity, potential temperature, salinity, and turbulence quantities. Häkkinen and Mellor [1992] applied the Princeton ocean model in a study of the seasonal variation of the Arctic ice-ocean system.

We shall later consider the ocean heat and salt balances, which are

$$\frac{\partial}{\partial t} T + \mathbf{u} \cdot \nabla T + w \frac{\partial}{\partial z} T = \frac{\partial}{\partial z} \left(K \frac{\partial}{\partial z} T \right) - \frac{(1-A)}{\rho c_p} \frac{\partial}{\partial z} I + \mathcal{F}_T \quad (15a)$$

$$\frac{\partial}{\partial t} S + \mathbf{u} \cdot \nabla S + w \frac{\partial}{\partial z} S = \frac{\partial}{\partial z} \left(K \frac{\partial}{\partial z} S \right) + \mathcal{F}_S \quad (15b)$$

where w is the vertical component of velocity, \mathcal{F}_T and \mathcal{F}_S represent horizontal diffusion, and K is a vertical diffusivity determined from turbulence closure. The absorption of short-

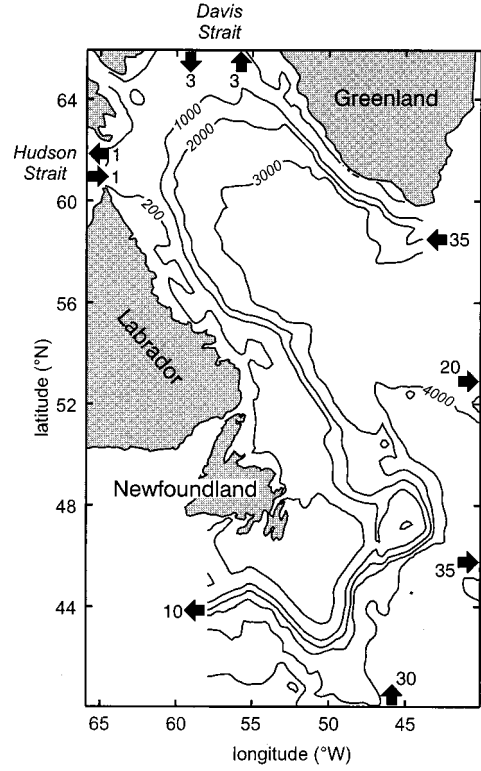


Figure 2. The model domain. The arrows indicate prescribed transports (sverdrups) at open boundaries. Depth contours are in meters.

wave radiation in the water column is expressed by the term involving I . Integrating (15) from $z = -D$ to the surface gives

$$\rho c_p \int_{-D}^0 \frac{\partial}{\partial t} T dz = \rho c_p \int_{-D}^0 \left(-\mathbf{u} \cdot \nabla T - w \frac{\partial}{\partial z} T + \mathcal{F}_T \right) dz - [(1-A)I(0) + F_T] - \rho c_p K \left. \frac{\partial}{\partial z} T \right|_{-D} \quad (16a)$$

$$\int_{-D}^0 \frac{\partial}{\partial t} S dz = \int_{-D}^0 \left(-\mathbf{u} \cdot \nabla S - w \frac{\partial}{\partial z} S + \mathcal{F}_S \right) dz - F_S - K \left. \frac{\partial}{\partial z} S \right|_{-D} \quad (16b)$$

where we have used surface boundary conditions for the vertical diffusive fluxes. We have also assumed in (16a) that D is sufficiently large such that $I(-D)$ is negligible. The three terms on the right-hand side of (16) are advection and horizontal diffusion, surface flux, and vertical diffusive flux (convective flux in winter) at $z = -D$.

2.4. Model Grid

The model equations are solved on the Earth's spherical coordinate system with a grid resolution of $1/5^\circ$ longitude and $1/6^\circ$ latitude. The model domain is shown in Figure 2. Bathymetry has been smoothed following the rationale and technique of Mellor *et al.* [1994]. The model uses 16 sigma levels in the vertical (0, -0.02, -0.04, -0.08, -0.17, -0.25, -0.33, -0.42, -0.50, -0.58, -0.67, -0.75, -0.83, -0.92, -0.96, and -1.00).

At open ocean boundaries we apply the flow relaxation scheme of *Martinsen and Engedahl* [1987]. The flow relaxation scheme requires a relaxation zone (chosen here as five grid intervals wide) in which the interior solution relaxes to values prescribed at the exterior boundary. For temperature and salinity, seasonal means interpolated to monthly values are prescribed. The normal component of the prescribed velocity is decomposed into baroclinic (zero depth average) and barotropic (no depth variation) components. The baroclinic component is determined from geostrophy. The barotropic component is derived from the transports indicated in Figure 2. The 35 Sv inflow south of Greenland determines the transport of the Labrador Current and is based on *Clarke* [1984]. The remaining transports are guesses of reasonable values.

Along the continuous eastern, southern, and western open boundary, sea level is specified from the normal component of surface velocity by geostrophy. To determine the sea level variation at the open boundaries across Davis Strait and Hudson Strait, a series of diagnostic runs (here chosen as three runs of 10 days duration each) is made. Sea level at the interior boundary at the end of the run serves as the prescribed boundary sea level for the subsequent run. The third diagnostic run and a 10 day prognostic run (no wind stress or surface heat flux) serve to spin up the ocean velocity. (The calculations presented here are for a prognostic ocean.) In a model study of the North Atlantic circulation, *Ezer and Mellor* [1994] found a timescale of 10–30 days for the dynamic adjustment of the density field to the bottom topography. Our model reaches a near-stationary state in the same timescale.

In the discrete version of (4) an ice category includes ice in a range of thicknesses. We select 10 categories that have central thickness 0, 0.12, 0.28, 0.52, 0.86, 1.32, 1.91, 2.54, 3.51, and 4.51 m. At Davis Strait we prescribe a monthly varying ice thickness to account for ice advected from outside the model domain. The prescribed ice thickness is a maximum of 1.81 m in February at the western end of the strait and decreases eastward. There is zero ice flux across the mouth of Hudson Strait.

2.5. Model Initialization and Forcing

The model is run from mid-November for a single ice season. Mean ocean temperature and salinity for November are obtained from an objective analysis of data [*Tang and Wang*, 1996]. The objective analysis uses an iterative difference correction procedure with topography-dependent radii of influence. The grid resolution is $1/6^\circ \times 1/6^\circ$. The data are extracted from the Atlantic Fisheries Adjustment Program temperature and salinity database archived at the Bedford Institute of Oceanography. The database covers an area from northern Baffin Bay to Cape Hatteras from the coast to 42°W and is derived from a variety of sources dating back to 1910 [*Petrie et al.*, 1996].

The initial ocean state following the diagnostic and prognostic spin-up is shown in Figure 3. Figure 3 shows that the shelf water is cold and fresh. At the surface the Labrador Current exceeds 0.3 m s^{-1} over the shelf break. The current extends to the bottom.

Monthly climatological data are used for the atmospheric forcing. Air temperature at 2 m, specific humidity at 2 m, precipitation, and cloudiness are taken from the NCEP/NCAR reanalysis [*Kalnay et al.*, 1996] and obtained from the National Oceanic and Atmospheric Administration (NOAA) Climate Diagnostics Center as monthly averages. The data are further

averaged over 23 years (1974–1996) to produce a monthly climatology.

Wind at 10 m and 6 hour interval \mathbf{u}_a (also from the NCEP/NCAR reanalysis) is used to derive monthly averages of $|\mathbf{u}_a|$, which is required for wind stress, and $|\mathbf{u}_a|$, which is required for heat fluxes. Over water the drag coefficient is calculated as a function of wind speed and air-sea temperature difference [*Smith*, 1988]. Over ice a constant drag coefficient of 2.3×10^{-3} is used. All atmospheric data are bilinearly interpolated to the model grid.

Sensible and latent heat fluxes are calculated using standard bulk formulae. Over water the sensible heat flux coefficient is calculated following *Smith* [1988]; over ice a constant value of 1.75×10^{-3} is used. The latent heat flux coefficient is set to 1.2 times the sensible heat flux coefficient [*Smith and Dobson*, 1984]. Evaporation is calculated from the latent heat flux. Shortwave radiation is calculated according to *Reed* [1977]. Shortwave radiation penetrates the water column. The penetration is based on Jerlov type 1A seawater [*Jerlov*, 1976] in which 31% of the radiation is absorbed below the first few meters, the absorption decaying exponentially with depth with a decay scale of 23.8 m. Net longwave radiation is calculated according to *Budyko* [1974].

3. Results

3.1. Seasonal Cycle of Ice

The evolution of the model and observed sea ice cover are shown in Figures 4 and 5, respectively, in which contours of ice concentration at monthly intervals are drawn. The observed ice concentration is derived from composite ice charts for the years 1963–1997 prepared by the Canadian Ice Service. The charts have been digitized at a resolution of 0.5° latitude by 1° longitude [*Prinsenberg et al.*, 1997]. The observed ice concentrations are medians for the observation period. The main features of the observed ice concentration are well represented by the model. Ice is largely confined to the shelf. The offshore ice edge shows little variation over the winter months. The maximum southward advance to $\sim 47^\circ\text{N}$ occurs in March. In spring, however, the model ice retreats more rapidly than the observed ice.

In Figure 6 we plot the seasonal evolution of model and observed ice extent south of 55°N . We define ice extent as the total area within the 10% concentration contour. The observed ice extents are monthly averages, again for the years 1963–1997, and are based on weekly composite ice charts. Figure 6 shows that the model and observed ice extent agree well during the growth phase. However, the model ice decays more rapidly than the observed. This is most evident in the decrease in extent between March and April.

Mean ice thickness \bar{h} in mid-March is drawn in Figure 7. Ice thickness is typically $< 0.4 \text{ m}$ south of 54°N . *Prinsenberg et al.* [1996] measured ice thickness from a helicopter-borne towed sensor. In the main pack ice east of Newfoundland in early March the peak in the ice thickness distribution was 0.7–0.8 m. The model ice thickness is underestimated.

Ikeda et al. [1996] reported results from a model with two categories: ice and open water. They found a typical ice concentration of 0.25. In the present model with multiple ice categories a dominant part of the ice cover has concentrations exceeding 0.9. The higher concentrations are closer to the observations. This suggests that the use of multiple ice categories, particularly the thermodynamic growth term, improves

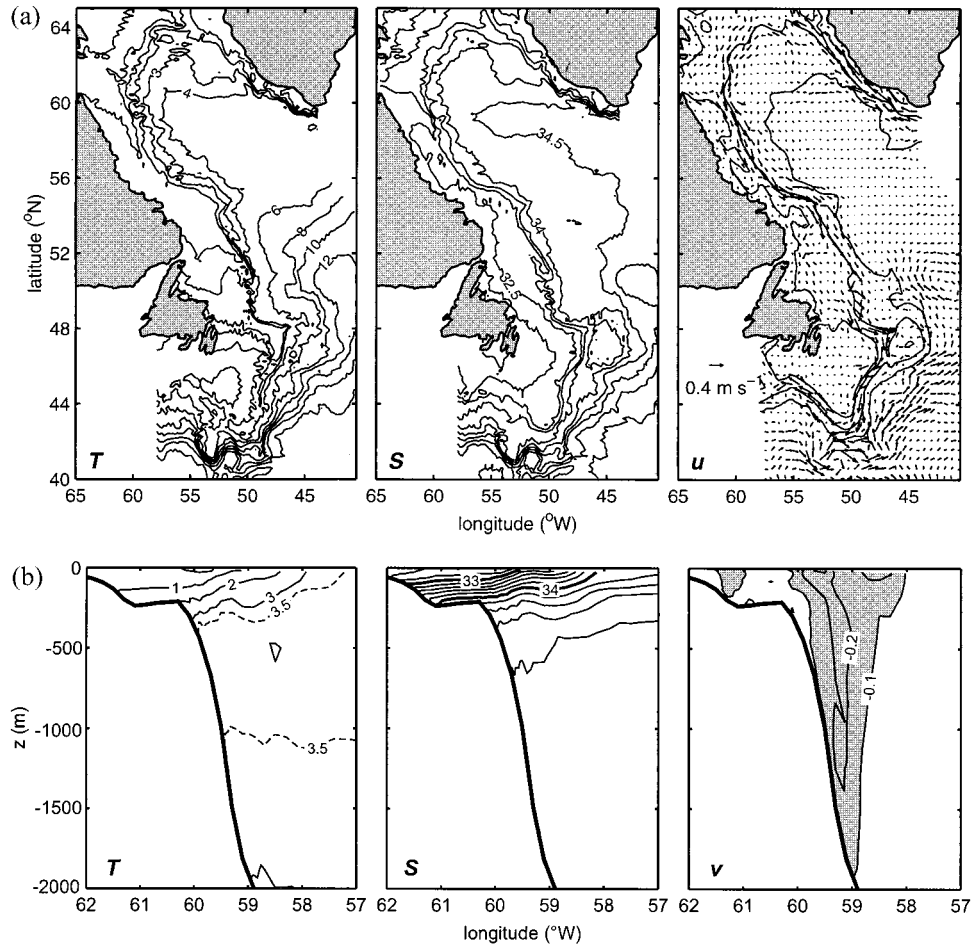


Figure 3. (a) Surface fields of temperature, salinity, and velocity initially (mid-November). The contour interval for temperature is 1°C below 4°C and 2°C above. The contour interval for salinity is 0.5. On the velocity plot model bathymetric contours of 200, 1000, and 3000 m are drawn. (b) Cross sections along 58°N of temperature, salinity, and the north component of velocity initially. The contour interval for salinity is 0.2. The contour interval for velocity is 0.1 m s⁻¹ with a velocity component of -0.1 m s^{-1} shaded.

upon the two-category model. The discrepancy between model and observation during the spring retreat was also encountered by Ikeda *et al.* [1996], who speculated that the two-category ice model was a contributing factor. The addition of a multicategory ice model does not eliminate the deficiency. In section 3.5 we show the heat source for the ice retreat, and in section 4 we discuss model sensitivity, particularly regarding the ice decay phase.

3.2. Ice Growth and Advection

The occurrence of ice arises from a combination of local growth and nonlocal advection (refer to (4)). In Figure 8 we show the separate contributions of ice formation and advection to the change in mean thickness \bar{h} . In Figure 8a we show total ice growth/melt over the 60 day period between mid-January and mid-March. Over the inner shelf, ice growth is positive. Over the outer shelf and slope the growth is negative, even during this period in which ice extent is increasing. A similar pattern of ice melt was shown by Ikeda *et al.* [1996]. The striking feature of Figure 8a is the large melt along a narrow strip at the offshore ice edge. At the ice edge, melt typically exceeds 2 m (and exceeds 4 m in places) over the 60 day period,

which is considerably larger than the thickness of the existing ice (Figure 7).

The ice melt requires there to be an influx of ice for the location of the ice edge to be maintained. In Figure 8b we show the change in ice thickness from advection and diffusion of ice over the same period. Figure 8b shows that over the inner shelf, there is divergence of the advective/diffusive ice flux; over the outer shelf, there is convergence of ice flux. The sign of the advection/diffusion term over most of the region opposes the sign of the growth. The magnitudes are in rough balance, which causes the cross-shelf ice distribution to remain nearly steady. (There is a slow increase in ice thickness over the season.)

Prinsenberg *et al.* [1991] inferred ice melt rates off Labrador and Newfoundland from ice charts and satellite-tracked beacons. Over the slope they found that the rate of ice melt in the vicinity of the edge reached a maximum of 0.22 m d⁻¹ with a mean of 0.11 m d⁻¹. The rate of ice melt was smaller over the shelf. Melt rates increased as the component of the ice velocity normal to the edge increased. The measurements of Prinsenberg *et al.* [1991] were located south of the region of large melt rate indicated in our model, but their melt rates correspond to

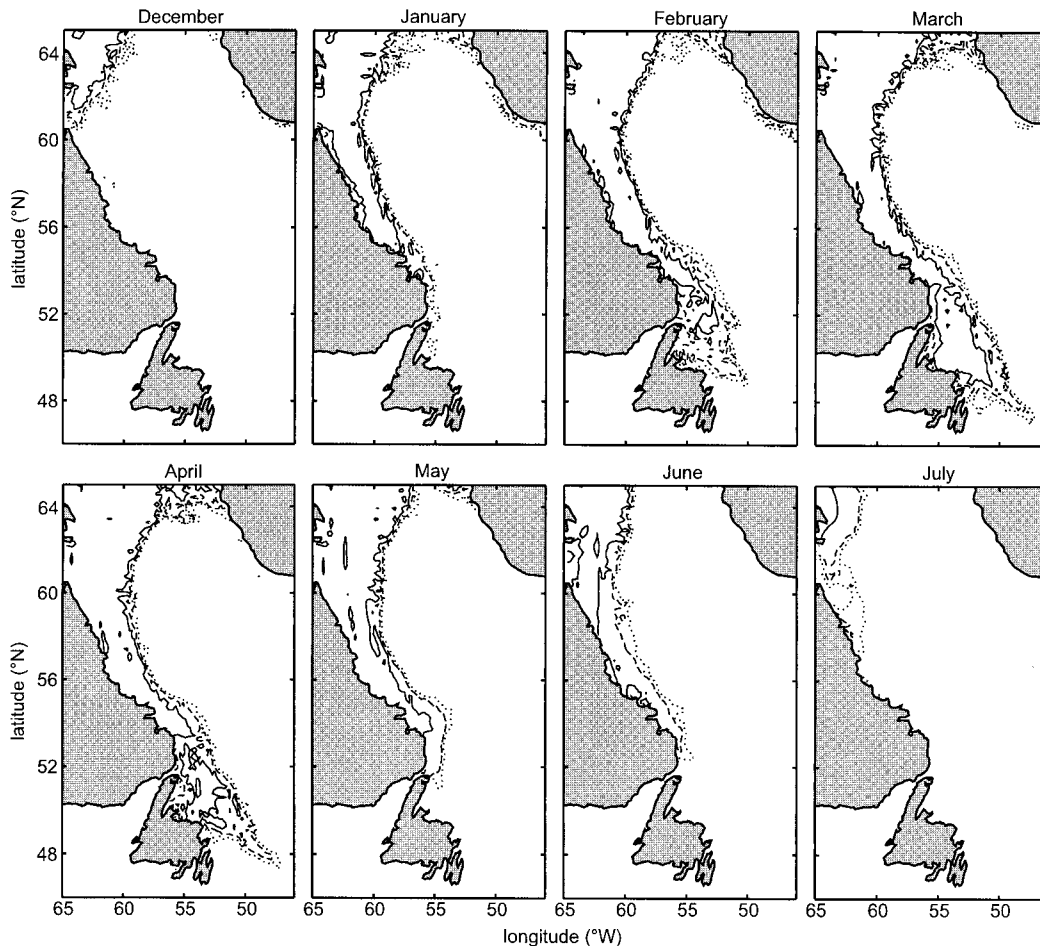


Figure 4. The seasonal evolution of model ice concentration. Concentrations are shown for the beginning of the indicated months. The contours are 0.1 (dotted line), 0.5 (dashed line), and 0.9 (solid line).

periods of a few days. Over these timescales, offshore ice velocities greater than those in our model could be sustained by synoptic winds.

Tang and deTracey [1998] computed ice melt rates from a coupled ice–mixed layer model and temperature–salinity data across the northeast Newfoundland shelf. They found the melt rates at the ice edge, $0.2\text{--}0.5\text{ m d}^{-1}$, were an order of magnitude higher than melt rates in the pack ice, $0\text{--}0.02\text{ m d}^{-1}$. These melt rates are instantaneous values, while the melt rates in Figure 8a are averages over a 2 month period.

The ice velocity field that gives rise to the pattern of advection in Figure 8b is shown in Figure 9. Figure 9 is a plot of the mid-February instantaneous ice velocity. Ice velocity, as well as the advective flux of ice, is dominantly alongshore. Figure 8b, however, shows that cross-shelf gradients determine the divergence of the advective/diffusive flux of ice. Near the ice edge, in the region of the large convergence of ice flux, gradients in ice thickness are also large (Figure 7). Peterson [1990] derived mean ice velocity fields from satellite imagery and ice beacon tracks. There is basic agreement between the model and observed ice velocity fields; the model field is spatially smoother than the observed field.

3.3. Ocean Heat Balance at the Offshore Ice Edge

In this section we consider the ocean heat balance in the vicinity of the offshore ice edge. In Figure 10a we draw the heat

loss from the ocean surface ($((1 - A)I(0) + F_T)$ (refer to (16a)) averaged over the 60 days from mid-January to mid-March. In the presence of ice, F_T contributes to melt according to (7) and (8). The remainder is lost to the atmosphere. Over the Labrador shelf, surface heat loss is $<100\text{ W m}^{-2}$. Offshore of the ice edge the heat loss ranges from 200 to over 400 W m^{-2} . Over a narrow strip along the ice edge, and coinciding with the maximum ice melt (Figure 8a), the heat loss is a maximum, typically exceeding 500 W m^{-2} .

Our interpretation of Figure 10a is that the presence of ice acts as an insulator reducing heat loss over the shelf. Offshore of the ice edge convection mixes the warm, deep water with the surface water. Melt at the ice edge causes the peak in the surface heat loss.

The question arises, What heat source balances the surface heat loss in the vicinity of the ice edge? In Figure 10b we draw the advection/horizontal diffusion term, integrated over the upper 100 m (refer to (16a)). The 100 m interval is chosen arbitrarily, but the results are qualitatively similar if the range of integration is a few hundred meters. The advection/horizontal diffusion also peaks along the ice edge and is opposite in sign to the surface heat flux. Figure 10 suggests that at the ice edge, heat lost from the surface is balanced by warming of the upper ocean from advection/horizontal diffusion.

In Figure 11a we draw profiles of the individual terms in the

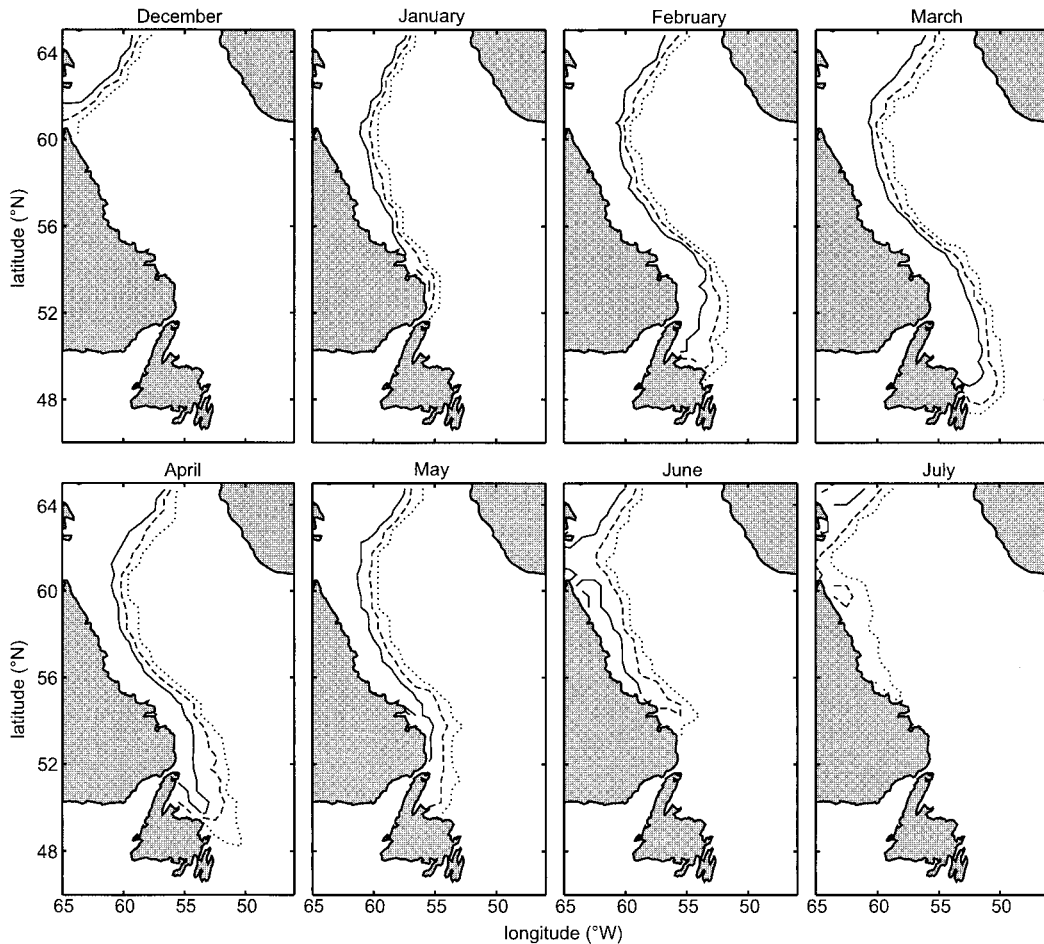


Figure 5. The seasonal evolution of observed ice concentration. Concentrations are shown for the beginning of the indicated months. The contours are 0.1 (dotted line), 0.5 (dashed line), and 0.9 (solid line).

heat balance (16a) along 58°N . The terms are averaged over the 60 day period between mid-January and mid-March, and (16a) is integrated over the upper 100 m. In Figure 11b we draw the temperature section along 58°N at mid-March. Con-

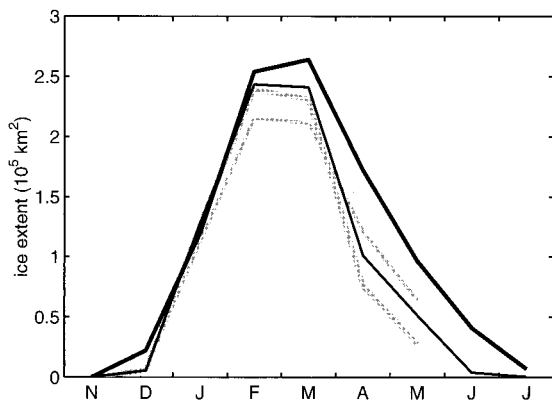


Figure 6. Model ice extent (thin solid line) and observed ice extent (thick solid line) south of 55°N . Also shown are the ice extents for two sensitivity experiments of section 4: experiment 2, ice at the northern boundary determined from interior ice (thick shaded line), and experiment 6, increased Labrador Current transport (thin shaded line).

sider first the region offshore of the ice edge (east of 58°W). The dominant terms in the heat balance are surface cooling and warming by convective mixing. By mid-March the extent of upper ocean mixing is evident, particularly between 55° and 58°W (Figure 11b). Next, consider the vicinity of the ice edge ($\sim 59^{\circ}\text{W}$). There is a peak in the surface heat loss. Ice melt here is nearly 8 m in 60 days, which accounts for the 400 W m^{-2} of the surface heat loss. Despite the large heat loss the temporal rate of change of temperature is small (equivalent heat flux $< 50 \text{ W m}^{-2}$). The ocean below the ice edge is stratified (the cold, fresh shelf water is less dense than the warm, salty offshore water), and convection is suppressed. The peak surface heat loss is balanced by advection/horizontal diffusion. Advection/horizontal diffusion transports heat from the convective region and helps the ice edge location remain constant (Figure 4). Finally, in the region beneath the ice cover (west of 60°W) the surface heat loss is reduced to below 100 W m^{-2} and is balanced by advection/horizontal diffusion.

Ikeda et al.'s [1996] study of the Labrador marginal ice zone portrays a similar picture of the ocean heat balance. A major difference is that our initial ocean state is more realistic and better resolves the shelf break front. *Ikeda et al.* [1996] used a data set that required the cold, fresh shelf water to be artificially specified. We have just seen the importance of the shelf break front on ice edge processes. The shelf break front is

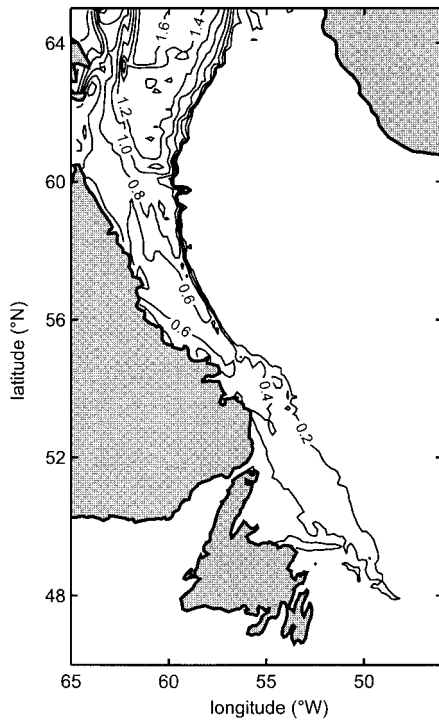


Figure 7. Mean ice thickness \bar{h} at mid-March. The contour interval is 0.2 m.

necessary for the stratified region under the ice edge, distinct from the convective well-mixed region offshore of the ice.

Houssais and Hibler [1992] discussed a two-dimensional model of the Greenland marginal ice zone. Our results show a

number of similarities. They found relatively large melt at the ice edge. The heat lost to melt at the ice edge was balanced by horizontal diffusion of heat in the ocean. There was a convective region offshore of the ice cover.

The mechanisms for the advective heat fluxes are beyond the scope of the present study. However, the region offshore of the ice edge is characterized by persistent model eddy activity. Eddies in this region are visible in satellite imagery [*LeBlond, 1982; Peterson, 1987*]. *LeBlond [1982]* suggested baroclinic instability as a likely generating mechanism.

3.4. Ocean Salt Balance at the Offshore Ice Edge

The ocean salt balance shows both similarities and differences with the heat balance. In Figure 12a we draw the individual terms of the salt balance (16b) along 58°N. Again, the terms are averaged over the 60 days between mid-January and mid-March, and (16b) is integrated over the upper 100 m. In Figure 12b we draw the cross section of salinity along 58°N at mid-March.

Offshore of the ice edge the temporal rate of change term is positive, primarily because of convection. The convective, well-mixed region (55°–58°W) is evident. Surface salt flux over open water is caused by precipitation minus evaporation. The surface flux, however, is minor compared with the convective flux. At the ice edge is the prominent peak in surface salt flux from ice melt. The peak is balanced by advection/horizontal diffusion. The temporal rate of change of salinity and the convection terms are small in comparison. The ocean beneath the ice edge is stratified by salinity. Under the ice cover there is ice formation over the inner shelf ($-F_s$ positive) and melt over the outer shelf ($-F_s$ negative). In response the temporal rate of change of salinity increases in the onshore direction. Advection/horizontal diffusion is important over the shelf, tend-

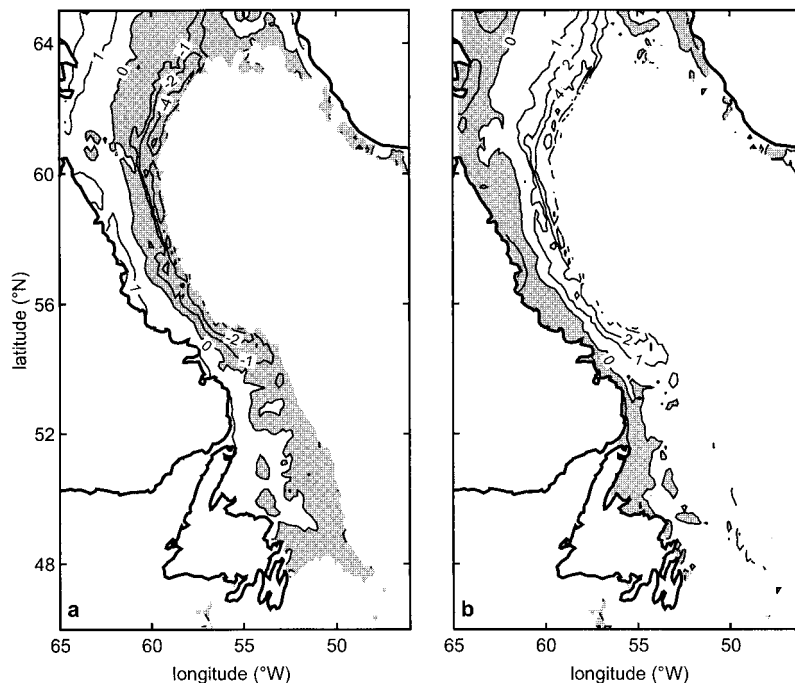


Figure 8. (a) Ice growth between mid-January and mid-March. (b) Ice advection and diffusion between mid-January and mid-March. For clarity the fields have been smoothed by a weighted average of nine adjacent grid points. The contours are -2 , -1 , 0 , 1 , and 2 m; outside this range the contour interval is 2 m. Negative regions are shaded.

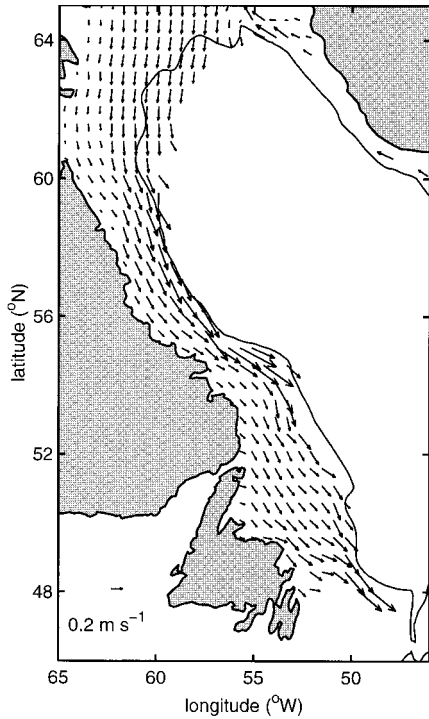


Figure 9. Ice velocity vectors from mid-February. The 1000 m depth contour is drawn.

ing to increase the salinity. The importance of alongshore advection of salt over the Newfoundland shelf was deduced by *Tang and deTracey* [1998], who compared results from an ice-mixed layer model with observed ocean temperature and salinity sections.

3.5. Retreat of Ice

Model ice retreat is more rapid than observed ice retreat. Comparing the relative importance of heat sources for the ice retreat may help to explain the discrepancy.

Add (6), (7), and (8) to obtain the rate of total ice growth:

$$\int_{0+}^{\infty} Q_{AI}(h)g(h)dh + (1-A)Q_{AW} - F_T = \rho L(W_{AI} + W_{IW} + W_{AW}). \quad (17)$$

Recall that Q_{AI} and Q_{AW} are the atmospheric heat fluxes excluding shortwave radiation over the open water fraction (refer to Figure 1). In the presence of ice the ocean surface heat loss F_T is given by (9), is nonnegative, and contributes to melt.

Let us consider the time period mid-March to mid-April. Figure 4 shows the ice retreat over this period. Figure 13 shows two of the terms of (17): total ice growth/melt and melt attributable to ocean heat loss. The terms are plotted along 50°N, which is representative of the retreat region. The melt attributable to ocean heat loss is the integral of F_T over the time at which ice is present and is converted to an equivalent ice melt. Figure 13 shows that ice growth along 50°N between mid-March and mid-April is negative; there is net ice melt. The difference between total ice growth and melt from ocean heat loss gives the remaining terms in (17): the growth attributable to the atmospheric heat fluxes Q_{AI} and Q_{AW} . This growth is positive and is important inshore where there is a region of open water and thus large $(1-A)Q_{AW}$. An examination of the individual terms on the right-hand side of (17) (not plotted) reveals that melt at the upper surface of ice W_{AI} is negligible compared with melt at the lower ice surface $W_{IW} + W_{AW}$.

Also shown in Figure 13 is the shortwave radiation over the open water fraction $(1-A)I(0)$. Again, this flux is integrated

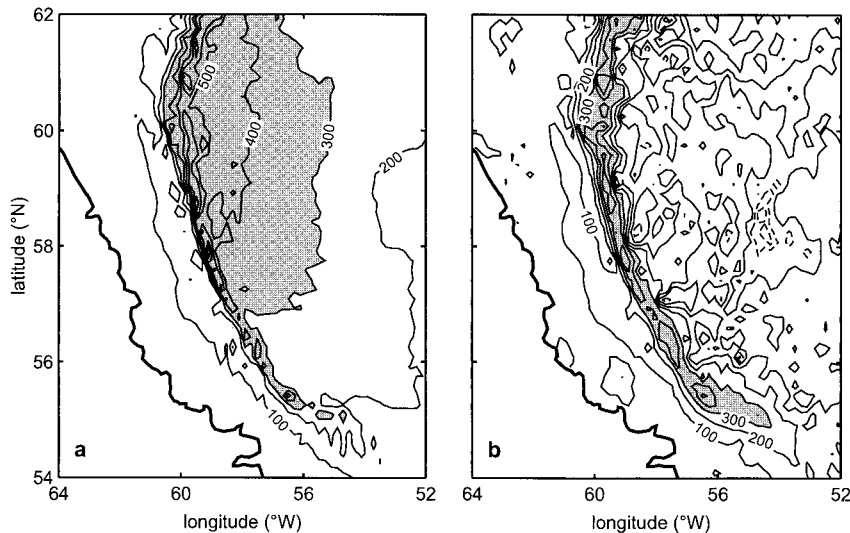


Figure 10. (a) Heat loss from the ocean surface $((1-A)I(0) + F_T)$ averaged between mid-January and mid-March. (b) Advection/horizontal diffusion of heat term in (16a) integrated over the upper 100 m and averaged between mid-January and mid-March. For clarity the advection field has been smoothed by a weighted average of nine adjacent grid points. The contour interval is 100 W m^{-2} , negative contours are drawn as dashed lines, and regions with heat flux exceeding 300 W m^{-2} are shaded.

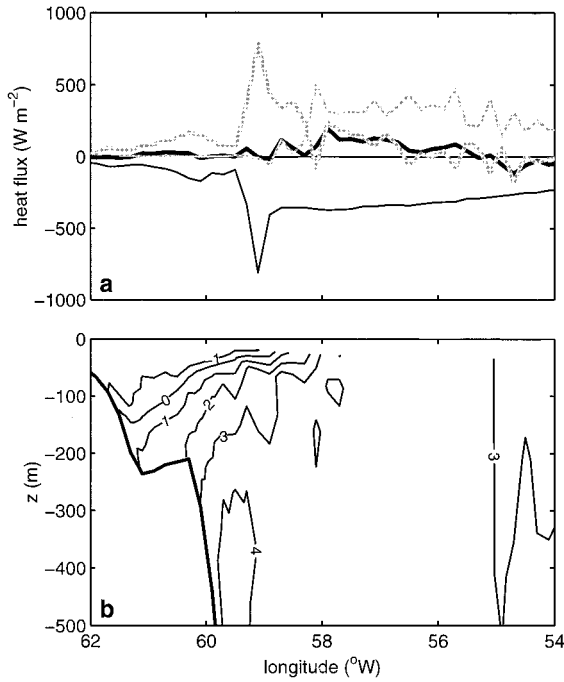


Figure 11. (a) Terms in the heat balance (16a) along 58°N: the rate of change (thick solid line), advection/horizontal diffusion (thick shaded line), surface flux (thin solid line), and convective flux (thin shaded line). The terms are averaged between mid-January and mid-March and are integrated over the upper 100 m. (b) The temperature section along 58°N for mid-March. The contour interval is 1°C.

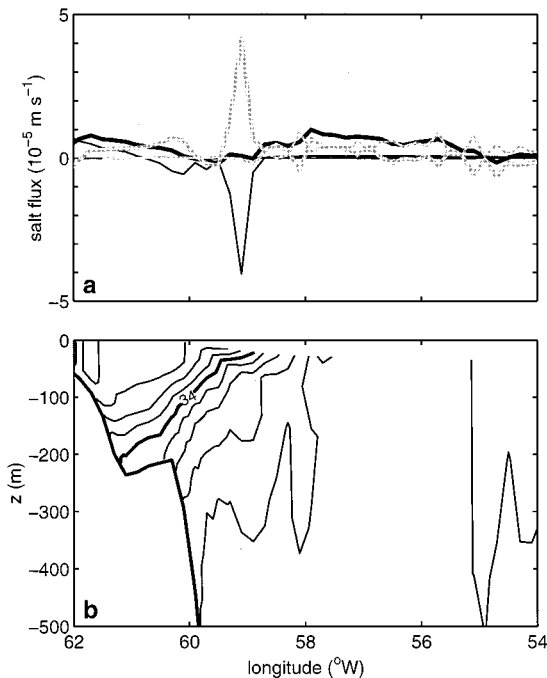


Figure 12. (a) Terms in the salt balance (16b) along 58°N: the rate of change (thick solid line), advection/horizontal diffusion (thick shaded line), surface flux (thin solid line), and convective flux (thin shaded line). The terms are averaged between mid-January and mid-March and are integrated over the upper 100 m. (b) Salinity section along 58°N for mid-March. The contour interval is 0.2.

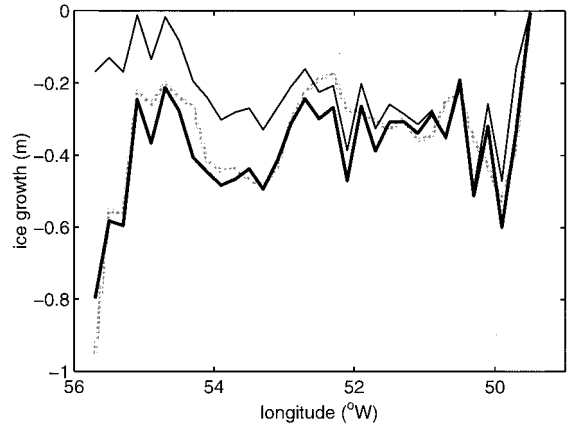


Figure 13. Total ice growth (thin line), ice melt attributable to ocean heat loss F_T (thick solid line), and shortwave radiation over the open water fraction converted to an equivalent ice melt (thick shaded line) between mid-March and mid-April along 50°N.

over the time that ice is present and converted to an equivalent ice melt. Figure 13 shows that $(1 - A)I(0)$ is the dominant contributor to F_T ; $(1 - A)I(0)$ nearly balances F_T in (16a). Shortwave radiation over the open water fraction is the dominant source of heat for ice melt during the retreat phase. That $(1 - A)I(0)$ causes ice melt at the same time that the remaining atmospheric heat fluxes Q_{AI} and Q_{AW} cause ice growth is related to the different albedo of snow/ice and ocean.

Typical melt rates from Figure 13 are 0.3 m in 30 days, which is equivalent to an average heat flux 30 W m^{-2} . This suggests that the retreat of ice may be sensitive to uncertainties in heat flux parameterizations. For example, uncertainties in solar radiation related to cloud fraction and cloud optical depth are of the order of 10 W m^{-2} [Bishop and Rossow, 1991]. The importance of $(1 - A)I(0)$ in ice melt implies that the retreat phase is also sensitive to the ice-covered fraction A .

4. Model Sensitivity

In this section we investigate the sensitivity of the results to certain model parameterizations and forcing. We focus particularly on the spring retreat of ice in the south, which is more rapid than the observed retreat. At the end of this section we

Table 1. Results of Sensitivity Experiments

Experiment*	March Volume, km ³	April Volume, km ³	March Extent, 10 ⁵ km ²	April Extent, 10 ⁵ km ²
1	60.5	40.1	2.41	1.01
2	54.5	26.2	2.31	0.76
3	83.1	72.6	2.49	1.15
4	59.2	40.7	2.41	1.08
5	60.8	41.1	2.48	1.18
6	62.7	50.9	2.11	1.21
7	60.5	54.4	2.41	1.74
observed			2.64	1.72

Experiments are 1, standard run; 2, ice at northern boundary specified from interior; 3, decrease ice strength parameter p^ ; 4, increase cloudiness in shortwave radiation; 5, modify heat flux in open water fraction; 6, increase transport of Labrador Current; and 7, decrease air temperature between March and April.

show results from a simulation with 6-hourly atmospheric forcing (as opposed to the climatological monthly averaged forcing we otherwise use).

Results are summarized in Table 1. Table 1 gives the ice volume and ice extent south of 55°N for March and April. Experiment 1 is the standard run described in the previous section. In experiment 1 we prescribe the ice thickness and concentration at Davis Strait, the northern boundary of the model domain. In experiment 2 we determine ice at the northern boundary from the interior solution (a zero gradient boundary condition). Ice extent south of 55°N is drawn in Figure 6. The difference is larger in April than in March; there is a lag for the ice introduced at the northern boundary to reach the southern part of the domain. The effect of the prescribed ice is to increase April ice extent from 0.76×10^5 to 1.01×10^5 km². Ice prescribed at the northern boundary has a significant effect, even south of 55°N .

In experiment 3 the ice strength parameter p^* in (2) is reduced to 5×10^3 N m⁻² from 2.5×10^4 N m⁻² for the standard run. The decreased ice strength decreases resistance to convergence and causes greater ice thickness. This is seen in the March ice volume, which increases from 60.5 to 83.1 km³ (an increase of 37%) while March ice extent increases from 2.41×10^5 to 2.49×10^5 km² (an increase of 3%). While model ice thickness in March is closer to *Prinsenberg et al.*'s [1996] measured values, ice thickness later in the season is unrealistically large. Thus an ice strength parameter $< 2.5 \times 10^4$ N m⁻² does not appear to be justified.

In experiment 4 we increase the cloudiness by 50% to a maximum of 1 in the shortwave radiation parameterization. The intent here is to show the effect of cumulative uncertainties in cloudiness, in the parameterization of shortwave radiation, and in albedo. In experiment 4, April ice extent increases a modest amount to 1.08×10^5 km². Uncertainty in shortwave radiation does not account for the discrepancy in the spring ice retreat.

In the standard run we specify that in ice-covered grid cells the surface temperature of the ocean is at the freezing point, and the heat flux out of the ocean is uniform over the grid cell. When (8) leads to "melting" of the open water fraction, the heat is distributed to the remaining ice categories, causing immediate melt. In experiment 5 we remove the constraint on the surface temperature of the open water fraction. The surface temperature is allowed to vary so that heat flux out of the ocean balances the heat flux to the atmosphere. In experiment 5 the April ice extent increases to 1.18×10^5 km². This suggests that the constraint on the surface temperature of the open water fraction is artificial and that it should be removed. Measurements of surface water temperature in the Newfoundland marginal ice zone [*Tang and deTracey*, 1998] indicate that the temperature is near freezing in the interior of the pack ice and increases toward the ice edge. In the transitional zone between pack ice and open ocean the surface temperature is between -1.5° and 0°C .

There is uncertainty in the magnitude and seasonal variation of the Labrador Current transport. In experiment 6 we increase the Labrador Current transport by 50% by modifying the inflow boundary condition south of Greenland. Ice extent south of 55°N is drawn in Figure 6. The results are mixed. The decrease in ice extent between March and April is 0.90×10^5 km², which is close to the observed decrease. The reduction in the rate of retreat is caused by increased southward advection of ice. However, the March ice extent is less than the standard

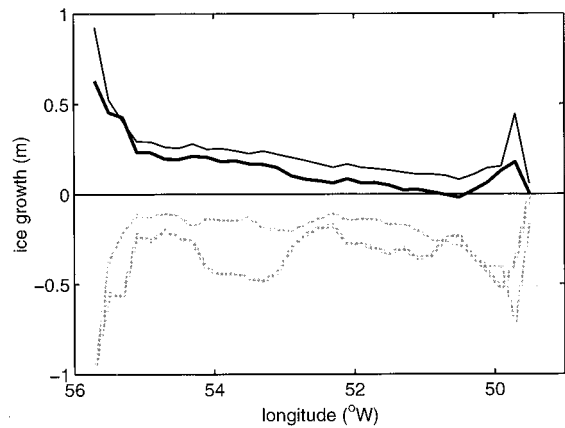


Figure 14. Shortwave radiation over the open water fraction converted to an equivalent ice melt (shaded lines) and ice growth attributable to the remaining atmospheric heat fluxes Q_{AI} and Q_{AW} (solid lines) between mid-March and mid-April along 50°N . The thick lines correspond to experiment 1, and the thin lines correspond to experiment 7.

case. Evidently, the increased ocean transport is associated with increased onshore advection of heat earlier in the ice season.

In experiment 7 we lower the air temperature by 2°C between mid-March and mid-April. The decrease in ice extent between March and April is 0.67×10^5 km², which is lower than the observed decrease (0.92×10^5 km²). The modeled ice now retreats more slowly than the observed ice. In Figure 14 we draw the ice growth/melt attributable to shortwave radiation over the open water fraction $(1 - A)I(0)$ and to the remaining atmospheric heat fluxes Q_{AI} and Q_{AW} between mid-March and mid-April along 50°N for experiments 1 and 7. The growth/melt is integrated over the time at which ice is present. With lower air temperature, ice growth attributable to Q_{AI} and Q_{AW} increases. This increase, however, is only part of the total change in growth. The melt attributable to $(1 - A)I(0)$ also decreases with lower air temperature by a comparable magnitude. This illustrates the sea ice albedo feedback. As ice melts, the open water fraction increases. The shortwave radiation over the open water fraction further increases the melt rate.

Smith and MacPherson [1996] have conducted airborne measurements in the atmospheric boundary layer above the marginal ice zone on the Newfoundland shelf. They find that under conditions of cold off-ice winds, there are strong lateral variations in wind, temperature, and vertical fluxes of heat and momentum. Temperature and heat flux consistently increase in the off-ice direction. The results are qualitatively consistent with the models of the atmospheric boundary layer over marginal ice of *Overland et al.* [1983] and *Kantha and Mellor* [1989].

An atmospheric boundary layer model gives variability in heat flux on the scale of the marginal ice zone. Experiment 7 suggests that a lower air temperature, as expected from an atmospheric boundary layer model, can delay the retreat of ice. Removing the constraint on the surface temperature of the open water fraction (experiment 5) also delays the retreat of ice.

Monthly atmospheric forcing may underestimate wind mixing related to storm events. We have conducted a model run with 6-hourly atmospheric forcing for the 1996–1997 ice sea-

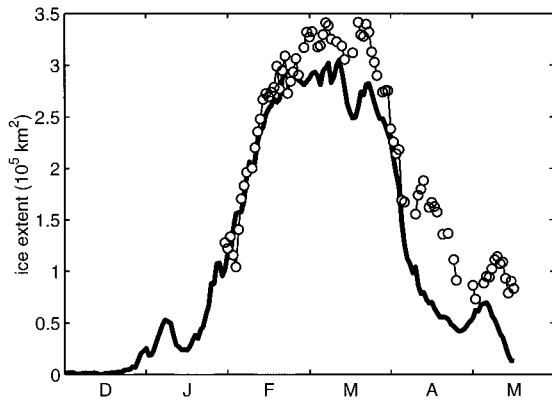


Figure 15. Model ice extent south of 55°N for the 1996–1997 ice season and 6-hourly atmospheric forcing (thick line) and observed ice extent (circles with thin lines, no lines where the separation in observations is >1 day).

son. The atmospheric forcing fields are from the Canadian Meteorological Centre regional weather forecasting model. The model parameters are as the standard run except that we have removed the constraint on uniform sea surface temperature and uniform surface ocean heat flux in grids containing ice (as in experiment 5). The model ice extent south of 55°N is drawn in Figure 15 together with the observed ice extent. The observed ice extent is derived from digitized daily analyses from the Canadian Ice Service. Figure 15 shares several features with the case of monthly atmospheric forcing (Figure 6). There is close agreement between model and observation in the ice growth phase. The model ice retreat is too rapid. The similarities suggest the validity of our use of climatological monthly atmospheric forcing to assess the model's ability to simulate the seasonal variation of ice and to investigate processes limiting the ice edge.

5. Conclusions

We have studied the seasonal cycle of ice offshore of Labrador with a coupled ice-ocean model, which is driven by monthly climatological atmospheric forcing. A significant improvement compared with previous studies, for example, *Ikeda et al.* [1996], should be the use of an initial ocean state from a data set that better resolves the gradients in ocean temperature and salinity at the shelf break. The model should give a better representation of the Labrador Current and of processes over the shelf and in the vicinity of the ice edge that rely on the shelf break stratification. We have also included multiple ice categories, which remedies a deficiency of *Ikeda et al.* [1996], where ice concentration was underestimated. The seasonal variation of ice in our model is quite realistic. This holds the potential for operational ice forecasting applications.

The results show that there is ice growth along the inner shelf and melt over the outer shelf. There is divergence of the advective/diffusive flux of ice over the inner shelf and convergence of the advective/diffusive flux of ice over the outer shelf, which maintains the location of the offshore ice edge. The vicinity of the ice edge is characterized by persistent, large melt, exceeding 1 m per month, and large heat flux out of the ocean, typically exceeding 500 W m^{-2} . At the ice edge the upper ocean is stratified, and convection is suppressed. Advection/horizontal diffusion transports heat from the convective

region to the region of the ice edge. An outstanding problem is the identification of the mechanism for the heat advection.

Shortwave radiation over the open water fraction is responsible for the spring retreat of ice at the southern limit. Ice melts predominantly at the bottom surface. Typical heat fluxes required to melt the ice are $<30 \text{ W m}^{-2}$. The model ice decay is too rapid compared with observations. We suggest that an appropriate treatment of the atmospheric boundary layer over ice can account for part of the discrepancy in the rate of ice decay.

Acknowledgments. This work was supported by the Panel for Energy Research and Development. We thank Jia Wang for help in model implementation and Brendan deTracey and Chou Wang for providing the meteorological and oceanographic data sets used. Simon Prinsenber and Brian Petrie read an early version of the paper and gave helpful comments and suggestions for improvement.

References

- Bishop, J. K. B., and W. B. Rossow, Spatial and temporal variability of global surface solar irradiance, *J. Geophys. Res.*, **96**, 16,839–16,858, 1991.
- Blumberg, A. F., and G. L. Mellor, A description of a three-dimensional coastal ocean circulation model, in *Three-Dimensional Coastal Ocean Models*, *Coastal Estuarine Sci.*, vol. 4, edited by N. S. Heaps, pp. 1–16, AGU, Washington, D. C., 1987.
- Bryan, K., A numerical method for the study of the circulation of the world ocean, *J. Comput. Phys.*, **4**, 347–376, 1969.
- Budyko, M. I., *Climate and Life*, 508 pp., Academic, San Diego, Calif., 1974.
- Carsey, F. D., S. A. Digby Argus, M. J. Collins, B. Holt, C. E. Livingstone, and C. L. Tang, Overview of LIMEX '87 ice observations, *IEEE Trans. Geosci. Remote Sens.*, **27**, 468–482, 1989.
- Clarke, R. A., Transport through the Cape Farewell-Flemish Cap section, *Rapp. P. V. Reun. Cons. Int. Explor. Mer.*, **185**, 120–130, 1984.
- Clarke, R. A., and J.-C. Gascard, The formation of Labrador sea water, I, Large-scale processes, *J. Phys. Oceanogr.*, **13**, 1764–1778, 1983.
- Cox, M. D., A primitive equation 3-dimensional model of the ocean, *GFDL Ocean Group Tech. Rep. 1*, 250 pp., Geophys. Fluid Dyn. Lab., Princeton, N. J., 1984.
- Drinkwater, M. R., and V. A. Squire, C-Band SAR observations of marginal ice zone rheology in the Labrador Sea, *IEEE Trans. Geosci. Remote Sens.*, **27**, 522–534, 1989.
- Ezer, T., and G. L. Mellor, Diagnostic and prognostic calculations of the North Atlantic circulation and sea level using a sigma coordinate ocean model, *J. Geophys. Res.*, **99**, 14,159–14,171, 1994.
- Flato, G. M., and W. D. Hibler, Ridging and strength in modeling the thickness distribution of Arctic sea ice, *J. Geophys. Res.*, **100**, 18,611–18,626, 1995.
- Häkkinen, S., and G. L. Mellor, Modeling the seasonal variability of a coupled Arctic ice-ocean system, *J. Geophys. Res.*, **97**, 20,285–20,304, 1992.
- Hibler, W. D., A dynamic thermodynamic sea ice model, *J. Phys. Oceanogr.*, **9**, 815–846, 1979.
- Hibler, W. D., Modeling a variable thickness sea ice cover, *Mon. Weather Rev.*, **108**, 1943–1973, 1980.
- Houssais, M.-N., and W. D. Hibler, Importance of convective mixing in seasonal ice margin simulations, *J. Geophys. Res.*, **98**, 16,427–16,448, 1993.
- Ikeda, M., T. Yao, and Q. Yao, Seasonal evolution of sea ice cover and shelf water off Labrador simulated in a coupled ice-ocean model, *J. Geophys. Res.*, **101**, 16,465–16,489, 1996.
- Jerlov, N. G., *Marine Optics*, 231 pp., Elsevier Sci., New York, 1976.
- Kalnay, E., et al., The NCEP/NCAR 40-year reanalysis project, *Bull. Am. Meteorol. Soc.*, **77**, 437–471, 1996.
- Kantha, L. H., and G. L. Mellor, A numerical model of the atmospheric boundary layer over a marginal ice zone, *J. Geophys. Res.*, **94**, 4959–4970, 1989.
- LeBlond, P. H., Satellite observation of Labrador Current undulations, *Atmos. Ocean*, **20**, 129–142, 1982.
- Martinsen, E. A., and H. Engedahl, Implementation and testing of a

- lateral boundary scheme as an open boundary condition in a barotropic ocean model, *Coastal Eng.*, *11*, 603–627, 1987.
- Mellor, G. L., User's guide for a three-dimensional primitive equation, numerical ocean model, 35 pp., Atmos. and Oceanic Sci. Program, Princeton Univ., Princeton, N. J., 1996.
- Mellor, G. L., and L. Kantha, An ice-ocean coupled model, *J. Geophys. Res.*, *94*, 10,937–10,954, 1989.
- Mellor, G. L., T. Ezer, and L.-Y. Oey, The pressure gradient conundrum of sigma coordinate ocean models, *J. Atmos. Oceanic Technol.*, *11*, 1126–1134, 1994.
- Overland, J. E., and C. H. Pease, Modeling ice dynamics of coastal seas, *J. Geophys. Res.*, *93*, 15,619–15,637, 1988.
- Overland, J. E., R. M. Reynolds, and C. H. Pease, A model of the atmospheric boundary layer over the marginal ice zone, *J. Geophys. Res.*, *88*, 2836–2840, 1983.
- Peterson, I. K., A snapshot of the Labrador Current inferred from ice-floe movement in NOAA satellite imagery, *Atmos. Ocean*, *25*, 402–415, 1987.
- Peterson, I. K., Sea ice velocity fields off Labrador and eastern Newfoundland derived from satellite imagery: 1984–1987, *Can. Tech. Rep. Hydrogr. Ocean Sci.*, *129*, 85 pp., 1990.
- Petrie, B., K. Drinkwater, D. Gregory, R. Pettipas, and A. Sandstrom, Temperature and salinity atlas for the Scotian Shelf and the Gulf of Maine, *Can. Tech. Rep. Hydrogr. Ocean Sci.*, *171*, 398 pp., 1996.
- Prinsenber, S. J., I. K. Peterson, and G. A. Fowler, Estimates of ice-edge melt rates off Labrador and eastern Newfoundland, Canada, *Ann. Glaciol.*, *15*, 163–170, 1991.
- Prinsenber, S. J., I. K. Peterson, and S. Holladay, Comparison of airborne electromagnetic ice thickness data with NOAA/AVHRR and ERS-1/SAR images, *Atmos. Ocean*, *34*, 185–205, 1996.
- Prinsenber, S. J., I. K. Peterson, S. Narayanan, and J. U. Umoh, Interaction between atmosphere, ice cover, and ocean off Labrador and Newfoundland from 1962 to 1992, *Can. J. Fish. Aquat. Sci.*, *54*, suppl. 1, 30–39, 1997.
- Reed, R. K., On estimating insolation over the ocean, *J. Phys. Oceanogr.*, *7*, 482–485, 1977.
- Smith, P. C., and J. I. MacPherson, Airborne surveys of the atmospheric boundary layer above the marginal ice zone on the Newfoundland shelf, *Atmos. Ocean*, *34*, 161–184, 1996.
- Smith, S. D., Coefficients of sea surface wind stress, heat flux, and wind profiles as a function of wind speed and temperature, *J. Geophys. Res.*, *93*, 15,467–15,472, 1988.
- Smith, S. D., and F. W. Dobson, The heat budget at Ocean Weather Station Bravo, *Atmos. Ocean*, *22*, 1–22, 1984.
- Tang, C. L., and B. M. deTracey, Space-time variation of mixed-layer properties, heat and salt fluxes, and ice melt in the Newfoundland marginal ice zone, *J. Geophys. Res.*, *103*, 1177–1191, 1998.
- Tang, C. L., and C. K. Wang, A gridded data set of temperature and salinity for the northwest Atlantic Ocean, *Can. Data Rep. Hydrogr. Ocean Sci.*, *148*, 45 pp., 1996.
- Tang, C. L., Q. Gui, and B. M. deTracey, A modeling study of upper ocean winter processes in the Labrador Sea, *J. Geophys. Res.*, *104*, 23,411–23,425, 1999.
- Thorndike, A. S., D. A. Rothrock, G. A. Maykut, and R. Colony, The thickness distribution of sea ice, *J. Geophys. Res.*, *80*, 4501–4513, 1975.
-
- I. K. Peterson, C. L. Tang, and T. Yao, Ocean Sciences Division, Fisheries and Oceans Canada, Bedford Institute of Oceanography, P.O. Box 1006, Dartmouth, Nova Scotia, Canada B2Y 4A2. (tyao@hp200ice.bio.dfo.ca)
- (Received January 15, 1999; revised June 9, 1999; accepted September 20, 1999.)

